

1 **Impact of gravity on directional solidification of refined Al-20wt.%Cu alloy investigated**  
2 **by *in situ* X-radiography**

3

4 Hadjer Soltani <sup>(a,c)</sup>, Fabiola Ngomesse<sup>(a)</sup>, Guillaume Reinhart <sup>(a)</sup>, Mohamed Chérif Benoudia<sup>(b)</sup>,  
5 Moussa Zahzouh<sup>(c)</sup> and Henri Nguyen-Thi <sup>(a)</sup>

6

7 <sup>a</sup> Aix Marseille University, CNRS, IM2NP, UMR 7334, Marseille, France

8 <sup>b</sup> Ecole Nationale supérieure des Mines et de la Métallurgie, L3M, Annaba, Algeria

9 <sup>c</sup> Badji Mokhtar University, LMGM, BP 12, 23000, Annaba, Algeria

10

11 **Abstract**

12 Gravity effects such as natural convection in the liquid phase and buoyancy forces acting  
13 on the solid phase have a strong influence on the grain structure and microstructure formation  
14 dynamics during the solidification of metal alloys. It is thus very useful to undertake  
15 experimental studies that will provide benchmark data for a deeper understanding of the role of  
16 such gravity effects. In this paper, we study the formation of the equiaxed grain structure during  
17 refined Al-20wt.%Cu solidification in a temperature gradient for three different configurations:  
18 horizontal, vertical upward and vertical downward solidification. The key grain characteristics,  
19 namely grain size, grain elongation and grain growth orientation, were determined for all  
20 experiments and a comparative study was performed to identify the dominant effects of gravity

21 for each case. The present study provides quantitative information on the impact of grain  
22 flotation and solute flows on the equiaxed microstructure characteristics by means of *in situ*  
23 laboratory X-radiography.

24

25 **Keywords:** Directional solidification, equiaxed microstructure, grain characteristics, *in situ* X-  
26 radiography, Al-Cu alloy, gravity, convection, buoyancy

27 **1. Introduction**

28 Metal material properties such as ductility and hardness are closely linked to the grain  
29 structure generated during solidification processes. Ever better understanding of grain structure  
30 dynamics during its development and of related underlying mechanisms is thus of utmost  
31 importance to control the growth conditions for engineering applications and to obtain pieces  
32 with the desired and reproducible properties. During solidification in a temperature gradient,  
33 two types of grain structure can form depending on the growth conditions (alloy composition,  
34 temperature gradient and cooling rate or sample pulling velocity): the columnar grain structure,  
35 with directional properties and the equiaxed grain structure with more uniform and isotropic  
36 properties. The equiaxed grain structure is the most used in aluminium-based industrial  
37 applications and can be promoted by inoculation, which consists in adding inoculant particles  
38 to the melt. These micrometer particles act as preferential sites for heterogeneous nucleation of  
39  $\alpha$ -Al grains, resulting in a uniformly fine, equiaxed as-cast microstructure [1, 2]. The same  
40 principle is also successfully applied to other metallic systems, notably magnesium and zinc  
41 alloys.

42 On Earth, gravity has a strong impact on the formation of solidification microstructures  
43 and makes the study of alloy solidification more complex because of the combination of  
44 multiple phenomena at different scales in time and space. Firstly, natural convection takes place  
45 in the melt and is the major source of various disturbing effects, which can significantly modify  
46 or mask other physical mechanisms [3-7]. Indeed, flows in the liquid modify the solute transport

47 in the melt, and generally prevent the formation of steady solidification patterns with uniform  
48 features. Thus, attempts have often been made to avoid convection in the melt in directional  
49 solidification studies to make easier the interpretation of the results [8]. A simple way of  
50 eliminating or reducing natural convection is to ensure that the density gradient in the liquid  
51 phase is vertical downward everywhere, the heavier liquid being at the bottom. This situation  
52 is more or less approached when growth occurs in a vertical upward temperature gradient, for  
53 an alloy system in which the rejected solute is denser than the solvent. For example, this is the  
54 case during upward directional solidification of hypo-eutectic Al-Cu alloys. However, even in  
55 this configuration, flow patterns adjacent to the solid-liquid interface can develop at low growth  
56 rates under the effect of a transverse horizontal temperature gradient that exists because of the  
57 difference in thermal conductivities of the solid phase, liquid phase and crucible wall. In that  
58 specific case, fluid flows can cause strong deformation (steeping and clustering phenomena)  
59 of the solid-liquid interface [9-11] and then large segregation in the material [12, 13]. For  
60 vertical downward solidification of hypo-eutectic Al-Cu alloys, both thermal and solutal  
61 gradients destabilize the liquid phase and strong convective motion in the melt are expected  
62 that can modulate macroscopically the solid – liquid interface, can delay or activate the  
63 morphological stability of the solid – liquid interface, and also leads to a significant longitudinal  
64 (parallel to the growth direction) macro-segregation [11, 14].

65 For vertical solidification experiments, regardless of the growth direction (upward or  
66 downward), an additional effect of gravity is buoyancy that acts on solid elements like dendrite

67 fragments and free grains. This force provokes either grain sedimentation or flotation,  
68 depending on the relative densities of the grain and the surrounding liquid [15-17]. It is worth  
69 noticing that buoyancy force acting on secondary dendrite arms also induces dendrite bending,  
70 leading in some cases to dendrite fragmentation [18].

71 Diffusive mass transport without any buoyancy effect can be achieved during microgravity  
72 experiments [17, 19-23], independently of alloy composition and container shape. However,  
73 such type of experiments is rare and very expensive, because of the limited number of  
74 microgravity opportunities. In normal gravity conditions, nearly diffusive conditions can be  
75 achieved by performing horizontal solidifications of very thin samples (down to 10  $\mu\text{m}$  in  
76 thickness), like in the case of transparent alloys solidification experiments [8]. In this  
77 experimental configuration, fluid flows are blocked by the strong confinement in one dimension.  
78 For metallic samples, it is very difficult to reduce the thickness down to 10  $\mu\text{m}$  in a uniform  
79 way and typical sample thickness is in the range 100-300  $\mu\text{m}$ . For this value, natural convection  
80 [17] and buoyancy effects [24] during horizontal solidification are largely, but not completely,  
81 reduced.

82 It is now well established that *in situ* and time-resolved study of solidification is relevant  
83 because most of the phenomena that occur during the process are dynamic. Various X-ray  
84 imaging methods have been developed in the last two decades, in particular using synchrotron  
85 radiation [25]. However, *in situ* X-radiography remains the most used method for studying  
86 metal alloy solidification because of its simplicity. X-radiography enables us to follow the

87 dynamics of the solid-liquid interface [26], the grain motion [27-29] and under certain  
88 conditions to determine quantitatively the solute concentration in the liquid phase [30, 31]. In  
89 the last decade, benefitting from the progress of microfocus X-ray sources and detectors,  
90 laboratory [32-35] as well as microgravity [17, 24, 36] apparatus have been developed to study  
91 *in situ* the solidification of metals. Even if microfocus X-ray sources do not generate a beam as  
92 powerful as synchrotron sources, they offer enough brilliance to conduct investigations of Al-  
93 based alloy solidification.

94 The aim of the present investigation is to examine and enlighten the major effects of gravity  
95 during the formation of an equiaxed microstructure in a fixed temperature gradient. For this  
96 purpose, directional solidifications of refined Al-20%Cu samples were carried out with  
97 different orientations of the sample with respect to the gravity direction, namely horizontal and  
98 vertical (upward and downward) solidifications. Experiments were performed in the SFINX  
99 (Solidification Furnace with IN Situ X-radiography) laboratory facility, which enabled us to  
100 follow the formation of the equiaxed microstructure using *in situ* X-radiography. The main grain  
101 and microstructure characteristics have been determined for all the experiments. Then, a  
102 comparative analysis between the various configurations has been conducted to emphasize the  
103 impact of natural convection as well as buoyancy force acting on the grains after nucleation  
104 during the formation of the equiaxed microstructure.

105

106

## 107 **2. Experiment description**

### 108 **2.1. SFINX apparatus**

109 Directional solidification experiments were performed in the SFINX (Solidification Furnace  
110 with IN Situ X-radiography) laboratory device, which is a duplicate of the facility used during  
111 several parabolic flight campaigns [36] as well as during the sounding rocket experiment  
112 MASER-12 [17]. These facilities were developed within the ESA (European Space Agency)  
113 project entitled XRMON (X-ray MONitoring of advanced metallurgical processes under  
114 terrestrial and microgravity conditions) to study the microstructure formation dynamics of  
115 metal alloys onboard of microgravity platform using X-radiography [37]. A detailed description  
116 of those facilities has been given in our previous papers [17, 19]. Only the main features are  
117 summarized below.

118 The dimensions of the sheet-like samples of refined Al-20wt.%Cu (0.1wt.%AlTiB) were 5 mm  
119 in width, 50 mm in length and 0.25 mm in thickness. The sample thickness was chosen in order  
120 to have a good transmission of the X-ray beam and prevent the superimposing of several grains  
121 at the same location so that the interpretation of radiographs is unambiguous. The polished  
122 sample was placed into stainless-steel spacers, sandwiched between two flexible glassy carbon  
123 sheets sewn together with a silica thread. The sample-crucible assembly was then installed  
124 inside the Bridgman-type furnace (Fig. 1a). The furnace consists of two identical heaters for the  
125 “hot” and “cold” zones that are independently regulated by a PID-regulator. During the  
126 experiments, the samples were directionally solidified by applying the same cooling rate  $R$  on

127 both heater elements, ensuring a fixed temperature gradient  $G$  during the entire experiment. The  
128 furnace enables directional solidification with temperature gradients within the range of 2.5-15  
129 K/mm and cooling rates  $R$  within the range of 0.01–1.5 K/s.

130 The X-radiography system features a microfocus X-ray source with a molybdenum target  
131 and a 3 mm focal spot (Fig. 1b). It provides a photon flux with two peaks of energy at 17.4 keV  
132 and 19.6 keV that ensure a good image contrast to study Al-Cu based alloys. The camera system  
133 is made of a scintillator plate that converts X-ray radiation to visible light and a digital camera  
134 with a CCD-sensor. As a result of the X-ray beam divergence, a geometric magnification of the  
135 object is observed at the detector, which is the ratio of the source-detector to source-object  
136 distances, the object in this case being the sample. In this work a magnification of  $\sim 5$  was  
137 obtained for a Field-of-View (FoV) of about  $5 \times 5 \text{ mm}^2$  and an effective pixel size of  $\sim 4 \times 4 \text{ }\mu\text{m}^2$ .  
138 The acquisition rate was 2 frames/second.

139 Grey level variations in the radiographs are related to the difference in X-ray absorption of the  
140 different parts of the sample, which depends mainly on the local density and composition.  
141 Image quality was enhanced by applying an image processing consisting in dividing each  
142 recorded frame by a reference picture recorded just before the beginning of the solidification  
143 [38]. After image processing, radiographs showed the equiaxed grains microstructure formed  
144 during the directional solidification of the refined Al-20wt.%Cu. Liquid regions of high copper  
145 concentration showed up as dark regions in the images, while  $\alpha$ -Al dendritic grains with low  
146 copper concentration were discernible as bright regions in the FoV [27, 30].



## 147 2.2. Experimental configurations

148 For comparison purposes, four refined Al-20wt.%Cu specimens were solidified with  
149 similar experimental parameters but with different orientations of the gravity vector. The  
150 furnace was set in two positions, allowing us to perform directional solidification experiments  
151 in three different configurations with respect to gravity: horizontal (1 sample), vertical upward  
152 (2 samples) and vertical downward (1 sample).

- 153 - *Case A*: the main surface of the sample was set perpendicular to the gravity vector  $\mathbf{g}$   
154 (Fig. 1b) and the solidification of the sample took place horizontally. In this  
155 experimental arrangement, the effects of gravity are expected to be strongly minimized.
- 156 - *Case B*: the samples were set in a vertical position by rotating the whole SFINX  
157 apparatus and the temperature gradient is anti-parallel to  $\mathbf{g}$  (bottom-up growth). During  
158 upward solidification of refined Al-20wt.%Cu alloy, both thermal and solutal gradient  
159 are stabilizing and natural convection is mainly due to the residual transverse  
160 temperature gradient [9, 10, 13]. Moreover, the impact of buoyancy on equiaxed grains  
161 will push the aluminum grains upward [28].
- 162 - *Case C*: with the same furnace position as in *Case B*, downward solidification of the  
163 sample was performed with a temperature gradient parallel to the gravity vector (top-  
164 down growth). In this case, both thermal and solutal gradients are destabilizing and  
165 strong convective flows are expected.

166

### 167 2.3. Solidification parameters

168 We solidified the refined Al-20wt.%Cu specimens in different gravity conditions, as  
169 described in the previous section, and with close growth parameters. **Table 1** summarizes the  
170 growth parameters of the experiments presented in this paper. The cooling rate value was  
171 identical for all the experiments,  $R = 0.15$  K/s, but the temperatures of the heater elements had  
172 to be adjusted for each configuration to achieve nearly the same average growth velocities and  
173 temperature gradients. Indeed, because of the asymmetry of the sample holder design as visible  
174 in **Fig. 1a** [19], the temperature interval between the two heater elements had to be increased  
175 by a factor two for the upward solidification experiments to obtain the same temperature  
176 gradient in the sample than for horizontal or downward solidifications. Furthermore,  
177 experiments with the same control parameters were carried out several times for each  
178 configuration to check the repeatability of the experiments and to improve our statistical  
179 analysis in terms of grain size, grain elongation and grain orientation (**cf. section 2.4**).

180 To determine accurate values of the growth parameters, we developed an experimental  
181 procedure based on the radiographs to measure in a first step the growth velocity [39]. The  
182 position of each grain in the FoV was marked manually as soon as they became visible  
183 (diameter  $\geq 10$ -20  $\mu\text{m}$ ) and the corresponding time was recorded. Then, the positions of the  
184 nucleation events were plotted as a function of time, and the average nucleation front velocity  
185  $\langle V_N \rangle$  can be easily derived from this plot. Assuming that the grain nucleation always occurs at  
186 a temperature close to the liquidus temperature in the case of refined alloys [40], the nucleation

187 front velocity was considered similar to the liquidus temperature velocity. The nucleation front  
188 velocity can be compared to the velocity of the eutectic front  $\langle V_E \rangle$  that crossed the FoV at the  
189 end of the solidification phase. A good agreement was obtained between the two types of  
190 measurement (see **Table 1**). Hereafter, the average nucleation front velocity  $\langle V_N \rangle$  will be used  
191 to compare the different experiments. In a second step, the actual temperature gradient was  
192 calculated using the relation  $G = R/V$ , which was assumed to be valid in our experiments.

193

#### 194 **2.4. Grain structure characterization**

195 A dendritic equiaxed microstructure was obtained during the cooling of the samples due to  
196 the AlTiB refining particles added into the alloy. By using X-radiography, the solidification was  
197 observed *in situ* with the equiaxed grain structure propagating from the cold zone to the hot  
198 zone. For each different configuration (horizontal, vertical upward and vertical downward  
199 solidifications), significant differences were observed for the solidification process as will be  
200 presented in the next sections. To analyze the gravity effects on the final grain structure, a  
201 quantitative analysis was conducted to determine the distribution of grain size, elongation and  
202 growth orientation for all experiments. The *in situ* observation of the solidification process  
203 allowed us to follow the microstructure formation and thus to measure the grain characteristics  
204 without any ambiguity. The first step consisted of contouring the grains one by one with the  
205 free software ImageJ [41] in order to obtain the grain surface area, using a semi-automatic  
206 macro script [39]. It was then possible to determine the distributions of grain size, grain

207 elongation and grain growth orientation:

- 208 - The grain size is defined as the diameter  $d$  of a disk having the same grain surface area,  
209 named equivalent disk (white circle in Fig. 2a). The grain surface area is easily  
210 retrievable since it is given by the ImageJ software in pixels. Even if the grain size is a  
211 very important parameter, it gives no information about the grain morphology and must  
212 be completed by other measurements.
- 213 - The grain elongation factor  $\phi$  is defined in a classical way by  $\phi = L_1/L_2$ , with  $L_1$  being  
214 the length of the longest straight segment inscribed within the grain and  $L_2$  the length of  
215 the longest straight segment inscribed within the grain and orthogonal to the segment  
216 that gives  $L_1$  (Fig. 2b). Both  $L_1$  and  $L_2$  were automatically obtained from the grain  
217 contouring using a macro in ImageJ. This definition is the inverse of the one used by  
218 Biscuola and Martorano [42] and the elongation factor varies in our paper from unity  
219 (for a perfectly equiaxed grain) to larger values (up to ten) for elongated grains.
- 220 - The growth orientation of each grain with respect to the temperature gradient direction  
221 was also measured. This grain orientation is characterized by the tilt angle  $\theta$  between  
222 the temperature gradient direction and the main dendrite axis (Fig. 2c). This third grain  
223 parameter is important to measure the impact of the temperature gradient on the growth  
224 direction. A wide  $\theta$ -distribution around a zero average value means that there is no  
225 preferential direction for the grain growth and thus that there is no influence of the  
226 temperature gradient on the grain growth direction.

227 It is worth noticing that similar information could be obtained by post-mortem microscopy,  
228 but only for the last solidification experiment since the samples were melted in between each  
229 solidification sequence.

230

### 231 **3. Case A: horizontal solidification**

#### 232 **3.1. Formation of the equiaxed grain structure**

233 **Fig. 3** shows a sequence of radiographs recorded during the experiments labelled A1 carried  
234 out in horizontal configuration. The solidification started with a fully melted sample and the  
235 application of the cooling rate on both heaters of the gradient furnace gave rise to the formation  
236 of grains in the cold zone of the furnace (**Fig. 3a**). Then, the solidification front propagated by  
237 wave-like nucleation ahead of the solidification front, in a similar way to the observations  
238 reported by many authors [43-46]. After their nucleation, the grains developed from almost the  
239 same initial location in the radiographs (**Fig. 3a**). By looking carefully at the grain dynamics, it  
240 was seen that some grains slightly rotated and seemed to move in the sample thickness. Many  
241 grains slightly moved towards the cold part of the sample due to solidification-induced  
242 shrinkage and interdendritic flow of the liquid phase as reported by Salloum et al. [28] for  
243 dendrite fragments. Those effects induced only very small grain motions and did not affect the  
244 key grain structure parameters. The entire solidification process can be seen in **Supplementary**  
245 **Video 1**.

246 After a short stage of rapid growth, the grains interacted with each other and gradually

247 formed a compact grain structure for which it was possible to define an effective front, at the  
248 top of the grain network (dashed line in Fig. 3c). This effective front separated the upper limit  
249 of the developing grain structure and the fully liquid phase. As the cooling of the sample  
250 continued, new layers of grains nucleated in the undercooled liquid zone ahead of the effective  
251 front (Fig. 3c). The new grains grew and eventually blocked the advancing effective front before  
252 being incorporated into the grain compact structure to form a new effective front. This  
253 mechanism was repeated over time (Fig. 3d), which lead to the formation of the equiaxed  
254 structure until the complete filling of the FoV (Fig. 3e). It is worth noticing that the grains were  
255 more elongated at the top of the FoV than in the bottom part. This was due to a higher  
256 longitudinal temperature gradient in this region close to the hot heater element of the furnace  
257 [39]. The remaining intra- and inter-dendritic liquid areas solidified at a later stage, following  
258 the crossing of the eutectic front through the FoV (dotted line in Fig. 3f).

259

### 260 **3.2. Grain structure characterization**

261 In Case A (horizontal solidification), the final grain structure in the FoV was composed of  
262 rather homogeneous and well dispersed grains. This was confirmed by the distributions of grain  
263 diameter (Fig. 4a), grain elongation factor (Fig. 4b) and grain growth orientation (Fig. 4c) for  
264 the experiment A1, which agrees with a recent detailed analysis of the impact of growth velocity  
265 on those distributions for a similar experimental configuration [39, 47]. The distribution of grain  
266 diameter was well-fitted by a Gaussian-type curve and the microstructure was rather

267 homogeneous in size in the FoV. For the grain size, the mean and maximal values were about  
268  $d_{peak} \sim 520 \mu\text{m}$  and the width at half height was  $\sigma = 170 \mu\text{m}$  (similar values were obtained for  
269 experiment A2). For the elongation factor, the distribution was well-fitted by a log-normal type  
270 curve, as shown in Fig. 4b. It can be seen that the largest number of grains had an elongation  
271 factor  $\phi$  lower than two (the maximum  $\phi_{peak}$  is about 1.4, with a width at half height  $\sigma=0.4$ ),  
272 which means that the grain structure was of equiaxed type, according to Hunt criterion [48]. A  
273 more detailed analysis of this histogram confirmed that the rare elongated grains ( $\phi > 2$ ) were  
274 mainly located in the top part of the FoV, in the region close to the hot heater element of the  
275 furnace where the temperature gradient was larger. Finally, the grain orientation distribution  
276 (Fig. 4c) was rather wide, with a peak at an angle  $\theta_{peak} \sim 9^\circ$ , which indicates that the grain  
277 orientation was not completely random as would have been expected for a perfectly equiaxed  
278 grain structure. The growth orientation was still influenced by the temperature gradient along  
279 the sample in these directional solidification experiments, as recently shown by H. Soltani *et al.*  
280 [39].

281

## 282 **4. Case B: Upward solidification**

### 283 **4.1. Impact of buoyancy on grain structure formation**

284 A sequence of radiographs recorded during the upward solidification experiment labelled  
285 B2 is shown in Fig. 5. The solidification parameters of this experiment were close to those of  
286 the experiment A1 described in the previous section (Table 1). The major difference between  
287 Case B and Case A was the impact of buoyancy force that induced the flotation of grains after

288 their nucleation (see [Supplementary Video 2](#)), due to the difference of densities between the  
289 solid and the liquid, the aluminum grains being much lighter than the surrounding Cu-rich liquid  
290 for equiaxed solidification of Al-20wt.% Cu alloys [49].

291 Because of buoyancy forces acting on all the nucleated grains, two different types of  
292 behavior were observed during the cooling of the sample. Firstly, some grains moved towards  
293 the hot part of the sample where they gradually melted, as described in detail in [28, 36] and  
294 clearly visible in the earlier stage of the experiment when there is still no well-defined equiaxed  
295 microstructure in the FoV. The upward motion of some grains is indicated by white arrows in  
296 [Fig. 5a](#) and this phenomenon can be seen more clearly in [Supplementary Video 2](#). The second  
297 type of grain behavior is specific to experiments carried out in thin samples (about 200  $\mu\text{m}$  in  
298 thickness). Due to the strong confinement, the upward motion of some grains could be stopped  
299 when their size was of same order than the sample thickness. When this occurred, they  
300 continued to develop roughly at the same location, like the pair of grains in plain circles in [Fig.](#)  
301 [5b](#) that remain visible in the subsequent radiographs. This “move-and-stop” behavior had two  
302 important effects on the final grain structure. Firstly, large residual liquid areas (rich of Cu)  
303 were forming in between the grains and lead to segregated regions like the one pointed out in  
304 [Fig. 5b](#) and [Fig. 5d](#). Subsequently, a few new grains nucleated in the residual liquid areas and  
305 moved upward until they were blocked by the previously stuck grains. The possibility of grain  
306 nucleation between growing grains has also been recently reported by Jia *et al.* during refined  
307 Al-15wt.%Cu alloy solidification [46]. In addition, another effect induced by gravity during



308 upward solidification was the promotion of dendrite fragmentations [50], leading to the  
309 development of many small grains inside the already grown microstructure.

310

## 311 **4.2. Grain structure characterization**

312 Grain size distribution, grain elongation factor and growth orientation angle are depicted  
313 in Fig. 6. Despite the impact of buoyancy forces acting on solid grains, the grain size  
314 distribution remained gaussian, with a peak value at about 520  $\mu\text{m}$ , which is surprisingly the  
315 same value than in the case of horizontal solidification. However, the width at half height was  
316  $\sigma = 260 \mu\text{m}$ , which is much larger than for horizontal solidification ( $\sigma = 170 \mu\text{m}$ ). For this  
317 experimental configuration, grains remained of equiaxed-type as shown by Fig. 6b, with  $\phi_{peak}$   
318 = 1.3, also close to the value of the horizontal case. The grain orientation distribution is wide,  
319 with a peak value at  $\theta = 8^\circ$ , which confirms that there is still a preferred grain orientation  
320 parallel to temperature gradient direction, despite the random motion and rotation of the  
321 equiaxed grains when floating.

322

## 323 **5. Case C: Downward solidification**

### 324 **5.1. Solute plumes observations**

325 For vertical downward solidification, the temperature gradient was parallel to the gravity  
326 vector, so that the temperature field was destabilizing regarding convective instabilities as the  
327 hot liquid was below the cold liquid. Moreover, the rejected solute (Cu) is heavier than the  
328 solvent (Al) yielding the solute to sink due to gravity and amplifying convective flow.

329 Thermosolutal convection is then expected to be the dominant gravity-driven effect in this case.  
330 **Fig. 7** depicts a sequence of radiographs of the experiment C1, showing the representative  
331 behaviour of all downward solidification experiments. In this experiment, an initially small  
332 porosity defect ( $\approx 80 \mu\text{m}$  in diameter) developed into a larger hole (around  $500 \mu\text{m}$  in width)  
333 visible at the bottom of the FoV as indicated in the first radiograph in **Fig. 7a**. The entering of  
334 the first grains in the FoV from the cold region of the sample is also visible **Fig. 7a**, as well as  
335 downward flows of Cu-rich liquid coming from the solidification microstructure and moving  
336 towards the bulk liquid (white arrows). These flows, also called convective plumes, were visible  
337 long before the appearance of the first grains in the FoV (readers are encouraged to see the  
338 **Supplementary Video 3**) and are caused by the rejection of heavy solute in the mushy zone  
339 during the solidification microstructure formation. In the radiographs, these plumes are visible  
340 because they are solute-rich and thus their X-ray absorption differs from the surrounding liquid  
341 at nominal composition.

342 Like in the previous experiments, the solidification microstructure progressed toward the  
343 hot part of the sample by wave-like nucleation mechanism. However, due to buoyancy force,  
344 the new solid grains floated and moved back against the existing solidification front and thus  
345 stopped rapidly the growth of existing grains (**Fig. 7b** to **Fig. 7e**). Accordingly, the equiaxed  
346 grains formed a dense and compact microstructure, whose characteristics were very different  
347 from the horizontal or upward solidification experiments due to gravity effects as discussed  
348 later in **section 5.3**. During the propagation of the solidification front, the plumes were drifting

349 continuously along the existing microstructure, as clearly visible in [Supplementary Video 3](#).  
350 Interestingly, solidification was delayed at the root of the segregated channel due to the local  
351 increase of solute composition ([Fig. 7b](#), [7c](#) and [7d](#)). The remelting of some small grains entering  
352 the Cu-rich channel was also observed (see [Supplementary Video 3](#)).

353

## 354 **5.2. Interaction between solute plumes and dendrite growth**

355 The impact of solute plumes on dendrite growth kinetic has been analyzed by means of X-  
356 radiography visualization. Using the ImageJ software, we were able to measure *(i)* the tip  
357 position of several dendrites and then to deduce their growth velocities as a function of time  
358 and *(ii)* the gray level in front of the dendrite tip. In our experiments, it was not possible to  
359 convert in a straightforward manner the gray level into solute concentration. However, the gray  
360 level values are related to the liquid concentration in front of the dendrite tip: the lower the gray  
361 level, the higher the liquid composition.

362 The studied dendrites were selected according to their growth direction, parallel to both  
363 gravity and temperature gradient, and their growth duration. For all the measured dendrites, it  
364 has been found that the dendrite tip velocity was strongly influenced by solute plumes passing  
365 in front of them, as illustrated in [Fig. 8](#). For the dendrite indicated in [Fig. 8a](#), we had the  
366 opportunity to reveal up clearly the interaction between the solute variation induced by solute  
367 plumes flows ([Fig. 8b](#)) and the dendrite tip growth velocity ([Fig. 8c](#)). In fact, the dendrite tip  
368 growth velocity oscillated above and below an average value, with a period of  $\approx 20$  seconds,

369 showing marked minimum and maximum. Comparing the two plots in Fig. 8 highlighted the  
370 close relationship between the dendrite tip growth velocity and the gray level variation. The  
371 variations of the dendrite tip velocity were approximately in phase with the liquid solute  
372 composition variations, i.e. the minimum and maximum of both curves occurred roughly  
373 simultaneously (as indicated by the dashed lines connecting the two curves). A maximum of Cu  
374 concentration in front of the dendrite tip gave a minimum of dendrite tip velocity. Moreover, in  
375 addition to the remarkable synchronization of these two curves, the oscillation amplitude  
376 variations were also in close accordance, at least qualitatively.

377

### 378 **5.3. Grain structure characterization**

379 When visually comparing the grain structure for Case C (downward solidification) with  
380 both other cases, the microstructure was found more compact, with both smaller and more  
381 elongated grains than for the horizontal and vertical upward solidifications.

382 Fig. 9a depicts the grain diameter distribution, which was not of gaussian type but well  
383 fitted by a log-normal function. The peak value for this experiment was about 184  $\mu\text{m}$ , which  
384 is nearly three times smaller than the value of the gaussian function of Case A or the average  
385 arithmetic mean of Case B. This log-normal distribution means that the grain structure was  
386 mainly composed of small grains completed by some longer grains. The more columnar aspect  
387 of the grain structure was confirmed by (i) the distribution of the elongation factor (Fig. 9b)  
388 that showed that the number of grains with an elongation factor higher than 2 was higher than

389 for horizontal or upward case and (ii) the distribution of tilt angle (Fig. 9c) that is of gaussian  
390 type with a prominent maximum close to 0°.

391

## 392 **6. Discussion**

393 The investigation of solidification experiments carried out with different orientations of the  
394 sample with respect to the gravity vector is an effective approach to highlight the impact of  
395 gravity-related phenomena on the solidification microstructure formation. Comparing vertical  
396 upward and downward experiment allows the impact of convective flow and buoyancy to be  
397 studied in thermo-solutally stabilizing or destabilizing configurations, as recently illustrated by  
398 Nelson *et al.* using *in situ* 4D synchrotron tomography for the solidification of an Al-15wt.%Cu  
399 alloy [51]. Valuable information can be obtained when such results are complemented by  
400 reference experiments performed in diffusive conditions, such as microgravity environment, as  
401 clearly demonstrated by Dupouy *et al.* [52] who investigated *post-mortem* the directional  
402 solidification of bulk hypo- and hyper-eutectic Al-Cu alloy. Although purely diffusive  
403 conditions were not achieved during the present work, the horizontal solidification experiments  
404 can be considered as reference cases for the comparison with the two vertical configurations.  
405 Indeed, in horizontal configuration buoyancy effects were strongly minimized by the  
406 confinement of the grain flotation in the small thickness of the sample. Thus, the grain motion  
407 was significantly restricted as reported in [24, 37] and numerically studied by [53]. In a same  
408 way, thermally and solutally induced convection was also expected to be significantly limited,

409 as previously discussed by Nguyen-Thi et al. using an order of magnitude analysis [50].

410 During the upward solidification experiments, the present observations show that the grain  
411 structure formation was disturbed mainly by the grain flotation due to buoyancy. This is at the  
412 origin of the non-homogeneous grain structure and wider distribution of the grain size. On one  
413 hand, the grains that moved towards the hot part of the sample and then melted did not  
414 participate to the final grain structure, thus leaving more space for the development both upward  
415 and on the sides of grains that remained stuck in the thickness. As a consequence, both larger  
416 and longer grains than in the horizontal case were obtained. It is worth noticing that the melted  
417 grains could strongly modify the solute composition of the bulk liquid phase, which for bulk  
418 samples such as ingot casting could be at the origin of strong macrosegregation. On the other  
419 hand, the growth of grains that nucleated in the residual liquid areas was restricted by the  
420 previously stuck grains, which resulted in the occurrence of smaller grains than in the horizontal  
421 case. The same went for the grains originating from dendrite fragments.

422 It is worth noting that buoyancy effects became negligible with the increase of cooling rate  
423 [47, 54]. Indeed, for a cooling rate of about 0.9 K/s (not shown in this paper), the growth  
424 velocity ( $\sim 120 \mu\text{m/s}$ ) and the grain flotation velocity ( $\sim 100 \mu\text{m/s}$ ) were of same order, yielding  
425 to an attenuation of the impact of flotation. Indeed, grains didn't have enough time to move  
426 upward after nucleation due to the rapid nucleation of a new layer of grains blocking their  
427 motion, leading the development of a grain structure similar to the one obtained in the horizontal  
428 case.

429 A visually striking feature of the downward experiments is the downward flows of Cu-rich  
430 liquid leading the formation of solute plumes that were continuously drifting along the effective  
431 solidification front. This non-stationary behavior may be attributed to the local change of the  
432 grain structure and its permeability during the growth process, yielding to a modification of the  
433 dissipative drag force exerted on the liquid and thus on the solute plumes [55]. Similar  
434 observations were also reported by Copley *et al.* [56] or Hellawell *et al.* [57] in transparent  
435 alloys, Hachani *et al.* [58] for Sn-3wt.%Pb alloy and more recently by Boden *et al.* [59] and  
436 Shevchenko *et al.* [32] during upward vertical solidification of Ga-In samples or Nelson *et al.*  
437 [51] during downward solidification of Al-Cu alloys.

438 The close link between dendrite tip velocity and solute plume motion ahead of the dendrite  
439 tip (Fig. 8) has been already mentioned by Shevchenko *et al.* [32] for the study of Ga-In, and  
440 more recently by Reinhart *et al.* [60] during directional solidification of superalloys. The  
441 explanation for these cycles running concurrently is that solute plumes locally increased the Cu  
442 concentration ahead of the dendrite tip, which reduced the constitutional undercooling intensity  
443 and thus slowed the dendrite tip growth [61].

444 By comparing the grain size orientation distributions of the three cases, it appears that the  
445 effect of the temperature gradient and of gravity on the grain morphology was stronger during  
446 downward experiments than for horizontal or upward experiments. During downward  
447 directional solidification of refined alloys, gravity impacts the grain structure dynamics by three  
448 distinct mechanisms. Firstly, there is the local increase of solute composition ahead of the

449 solidification front due to the solute plumes that reduces the constitutional undercooling  
450 intensity in front of the equiaxed structure. This modifies not only the dendrite tip velocity as  
451 discussed above but also provoked an inhibition of refiners. As a result, no nucleation of new  
452 grains was observed in the close vicinity of the solute plumes and the already existing grains  
453 have become more elongated. We can also mention that solute plumes could also change the  
454 spatial distribution of refining particles. However, this effect could not be analyzed in our  
455 experiments. Secondly, a subtler effect of gravity on grain structure formation is caused by the  
456 sinking of the Cu-enriched liquid, which stretches the solute boundary. The dilation of iso-  
457 concentrations has been also put forward by Bogno *et al.* [62] to explain the difference in  
458 behavior, in terms of velocity and length, of the upward and downward arms of equiaxed grains  
459 growing in isothermal conditions but in a vertical sample. Consequently, liquid undercooling  
460 ahead of the existing grain structure becomes less intense, yielding to a reduction of the grains  
461 nucleation rate and then augmenting the growth period. A third effect comes from the fact that  
462 the grains did not nucleate directly in front of the growing dendrite tips, but often appeared on  
463 their sides. Those grains moved toward the solidification front due to buoyancy effect and were  
464 trapped in the mushy zone, in between grains that were already developing. The consequence  
465 of these combined effects was that long grains of several millimeters could easily develop  
466 toward the bottom of the FoV without being blocked, while the growth of grains trapped in the  
467 mushy zone was stopped, which agrees well with the measurement of both small equiaxed  
468 grains and long columnar dendrites as shown in [Fig. 9](#).



469 Finally, it can be mentioned that the formation of segregated channels in the mushy zone  
470 was not observed in our experiments as (i) either the secondary arms of dendrites on both sides  
471 of the plumes grew more rapidly than the average transport of solute or (ii) free equiaxed grains  
472 moved upward and plugged the root of the plumes (see [Supplementary Video 3](#)). Only a residual  
473 liquid area developed above the porosity ([Fig. 7d](#)) and lead the formation of a segregated area.  
474 For a sake of completeness, we can mention that stable liquid channels on one side of the sample  
475 were observed during downward solidification of refined Al-20wt.%Cu alloys with the  
476 application of permanent magnetic field [63]. In those experiments, it has been demonstrated  
477 that an additional thermo-electro-magnetic force pushes the Cu-enriched liquid in the transverse  
478 direction of the sample. As a result, a liquid channel was created on one side of the sample,  
479 depending on the magnetic field direction.

480

## 481 **7. Conclusion**

482 Gravity effects on equiaxed solidification were investigated during horizontal, vertical  
483 upward and vertical downward directional solidifications of refined Al-20wt.%Cu (0.1wt.%  
484 AlTiB) samples. The solidification has been provoked by lowering the temperature of both  
485 heater elements and the observation of the grain structure has been done *in situ* and in real-time  
486 by X-radiography using the SFINX laboratory facility. The comparison between the three  
487 experimental configurations enlightened the marked effects of gravity on the grain structure  
488 formation and then on the final grain structure:

489 - For upward solidification, the dominant effect was buoyancy that provoked the grain  
490 flotation in the case of Al-20wt.%Cu alloy and caused the formation of liquid pockets at low  
491 growth rates. The grain motion following the nucleation phase yielded a non-homogeneous  
492 grain structure.

493 - For downward solidification, the most striking effect was the formation of solute flow, also  
494 called solute plumes. These fluid flows strongly affected the dendrite growth kinetic, which  
495 oscillated in phase with solute variations in the liquid ahead of the dendrite tips. Moreover,  
496 the local increase in solute due to the plumes prevented grain nucleation in their close vicinity.  
497 Another influence of gravity is related to buoyancy that kept the grains very close to the  
498 downward growing microstructure and then significantly shortened their growth duration.  
499 As a result, the average grain size was three times smaller for this type of experiment than  
500 for horizontal or upward solidifications.

501 All these gravity-driven effects have been observed only at low growth rates. For higher growth  
502 rates, neither grain flotation nor solute plume movement affected the microstructure.

503 To continue the study and overcome the gravity effects, a microgravity solidification  
504 experiment was conducted on board of the sounding rocket MASER-14 in June 2019 to obtain  
505 benchmark experimental data. The columnar-to-equiaxed transition was investigated during  
506 this campaign, for a grain-refined Al-20wt.%Cu sample, which is also the alloy composition  
507 used in this paper. A comparison will be made between the experiments carried out in  
508 microgravity and on ground, as the one presented in this paper, to investigate further the impact

509 of gravity and allow a reliable comparison with numerical simulations.

510

## 511 **Acknowledgements**

512 This work is supported by the XRMON project (AO-2004-046) of the MAP program of  
513 the European Space Agency (ESA), by the French National Space Agency (CNES) and the  
514 French-Algerian doctoral fellowship program PROFAS B+. The authors would also like to  
515 thank the Swedish Space Corporation (SSC) for the development of the SFINX facility and the  
516 technical support.

517

## 518 **Appendix A. Supplementary data**

519 Supplementary data related to this article can be found at ([link to supplementary material](#))

520

## 521 **References**

- 522 [1] T.E. Quisted, Understanding mechanisms of grain refinement of aluminium alloys by inoculation, *Materials*  
523 *Science and Technology* 20(11) (2004) 1357-1369.
- 524 [2] J.A. Spittle, Columnar to equiaxed grain transition in as solidified alloys, *Int. Mater. Rev.* 51(4) (2006) 247-269.
- 525 [3] M.D. Dupouy, B. Drevet, D. Camel, Influence of Convection on the Selection of Solidification Microstructures  
526 at Low Growth Rates, *J. Cryst. growth* 181 (1997) 145-159.
- 527 [4] S.R. Coriell, M.R. Cordes, W.J. Boettinger, R.F. Sekerka, Convective and interfacial instabilities during  
528 unidirectional solidification of a binary alloy, *Journal of Crystal Growth* 49(1) (1980) 13-28.
- 529 [5] G.B. McFadden, R.G. Rehm, S.R. Coriell, W. Chuck, K.A. Morrish, Thermosolutal Convection During Directional  
530 Solidification, *Metallurgical Transactions a-Physical Metallurgy and Materials Science* 15(12) (1984) 2125-2137.
- 531 [6] M.E. Glicksman, S.R. Coriell, G.B. McFadden, Interaction of flows with the crystal-melt interface, *Ann. Rev.*  
532 *Fluid Mech.* 18 (1986) 307.
- 533 [7] S.H. Davis, Hydrodynamics Interactions in Directional Solidification, *J. Fluid Mech.* 212 (1990) 241-262.
- 534 [8] S. Akamatsu, H. Nguyen-Thi, In situ observation of solidification patterns in diffusive conditions, *Acta Mater.*  
535 108 (2016) 325-346.
- 536 [9] M.H. Burden, D.J. Hebditch, J.D. Hunt, Macroscopic Stability of a planar, cellular or dendritic interface during

537 directional freezing, *J. Cryst. Growth* 20 (1973) 121-124.

538 [10] H. Nguyen-Thi, Y. Dabo, B. Drevet, M.D. Dupouy, D. Camel, B. Billia, J.D. Hunt, A. Chilton, Directional  
539 Solidification of Al-1.5wt% Ni alloys under diffusion transport in space and fluid flow localisation on Earth, *J. of*  
540 *Crystal Growth* 281 (2005) 654-668.

541 [11] J.D. Verhoeven, J.T. Mason, R. Trivedi, The Effect of Convection on the Dendrite to Eutectic Transition, *Metall.*  
542 *Trans. A* 17A (1986) 991-1000.

543 [12] A. Bogno, G. Reinhart, A. Buffet, H. Nguyen Thi, B. Billia, T. Schenk, N. Mangelinck-Noël, N. Bergeon, J.  
544 Baruchel, In situ analysis of the influence of convection during the initial transient of planar solidification, *Journal*  
545 *of Crystal Growth* 318(1) (2011) 1134-1138.

546 [13] A. Bogno, H. Nguyen-Thi, A. Buffet, G. Reinhart, B. Billia, N. Mangelinck-Noël, N. Bergeon, J. Baruchel, T.  
547 Schenk, Analysis by synchrotron X-ray radiography of convection effects on the dynamic evolution of the solid-  
548 liquid interface and on solute distribution during the initial transient of solidification, *Acta Mater.* 59(11) (2011)  
549 4356-4365.

550 [14] H. Jamgotchian, B. Billia, L. Capella}, Interaction of thermal convection with the solid-liquid interface during  
551 downward solidification of Pb-30wt%Ti alloys, *J. of Crystal Growth* 85(3) (1987) 318-326.

552 [15] H. Nguyen-Thi, A. Bogno, G. Reinhart, B. Billia, R.H. Mathiesen, G. Zimmermann, Y. Houltz, K. Löth, D. Voss,  
553 A. Verga, F.d. Pascale, Investigation of gravity effects on solidification of binary alloys with in situ X-ray radiography  
554 on earth and in microgravity environment, *Journal of Physics: Conference Series* 327(1) (2011) 012012.

555 [16] G. Reinhart, H. Nguyen Thi, J. Gastaldi, B. Billia, N. Mangelinck-Noël, T. Schenk, J. Härtwig, J. Baruchel, In situ  
556 and real time investigation of directional solidification  
557 of Al - Ni alloys by synchrotron imaging, *Materials Science Forum* 508 (2006) 75-80.

558 [17] H. Nguyen-Thi, G. Reinhart, G.S. Abou Jaoude, R.H. Mathiesen, G. Zimmermann, Y. Houltz, D. Voss, A. Verga,  
559 D.J. Browne, A.G. Murphy, XRMON-GF: A novel facility for solidification of metallic alloys with in situ and time-  
560 resolved X-ray radiographic characterization in microgravity conditions, *Journal of Crystal Growth* 374 (2013) 23-  
561 30.

562 [18] G. Reinhart, H. Nguyen-Thi, N. Mangelinck-Noel, J. Baruchel, B. Billia, In Situ Investigation of Dendrite  
563 Deformation During Upward Solidification of Al-7wt.%Si, *JOM* 66(8) (2014) 1408-1414.

564 [19] A.G. Murphy, G. Reinhart, H. Nguyen-Thi, G.S. Abou Jaoude, D.J. Browne, Meso-scale modelling of directional  
565 solidification and comparison with in situ X-ray radiographic observations made during the MASER-12 XRMON  
566 microgravity experiment, *Journal of Alloys and Compounds* 573 (2013) 170-176.

567 [20] F.L. Mota, N. Bergeon, D. Turret, A. Karm, R. Trivedi, B. Billia, Initial transient behavior in directional  
568 solidification of a bulk transparent model alloy in a cylinder, *Acta Mater.* 85 (2015) 362-377.

569 [21] D.R. Liu, N. Mangelinck-Noel, C.A. Gandin, G. Zimmermann, L. Sturz, H. Nguyen-Thi, B. Billia, Simulation of  
570 directional solidification of refined Al-7 wt.%Si alloys - Comparison with benchmark microgravity experiments,  
571 *Acta Mater.* 93 (2015) 24-37.

572 [22] D.R. Liu, N. Mangelinck-Noel, C.A. Gandin, G. Zimmermann, L. Sturz, H.N. Thi, B. Billia, Structures in  
573 directionally solidified Al-7 wt.% Si alloys: Benchmark experiments under microgravity, *Acta Mater.* 64 (2014) 253-  
574 265.

575 [23] Y.Z. Li, N. Mangelinck-Noël, G. Zimmermann, L. Sturz, H. Nguyen-Thi, Comparative study of directional  
576 solidification of Al-7 wt% Si alloys in Space and on Earth: Effects of gravity on dendrite growth and Columnar-to-

577 equiaxed transition, *Journal of Crystal Growth* 513 (2019) 20-29.

578 [24] A.G. Murphy, R.H. Mathiesen, Y. Houltz, J. Li, C. Lockowandt, K. Henriksson, G. Zimmermann, N. Melville, D.J.  
579 Browne, XRMON-SOL: Isothermal equiaxed solidification of a grain refined Al–20 wt%Cu alloy, *Journal of Crystal*  
580 *Growth* 440 (2016) 38-46.

581 [25] J. Baruchel, M. Di Michiel, T. Lafford, P. Lhuissier, J. Meyssonier, H. Nguyen-Thi, A. Philip, P. Pernot, L. Salvo,  
582 M. Scheel, Synchrotron X-ray imaging for crystal growth studies, *Comptes Rendus Physique* 14(2–3) (2013) 208-  
583 220.

584 [26] R.H. Mathiesen, L. Arnberg, H. Nguyen-Thi, B. Billia, In Situ X-Ray Video Microscopy as a Tool in Solidification  
585 Science, *JOM* 64(1) (2012) 76-82.

586 [27] L. Abou-Khalil, J. Wang, G. Salloum-Abou-Jaoude, M. Garrido, X. Li, Z. Ren, G. Reinhart, H. Nguyen-Thi, Y.  
587 Fautrelle, Investigation of Thermo-Electro-Magnetic force on equiaxed grain motion during upward directional  
588 solidification, *International Journal of Thermal Sciences* 145 (2019) 106047.

589 [28] G. Salloum-Abou-Jaoude, H. Nguyen-Thi, G. Reinhart, R.H. Mathiesen, G. Zimmermann, D. Voss,  
590 Characterization of motion of dendrite fragment by X-ray radiography on Earth and under microgravity  
591 environment  
592 *Materials Science Forum* 790-791 (2014) 311-316.

593 [29] A.G. Murphy, W.U. Mirihanage, D.J. Browne, R.H. Mathiesen, Equiaxed dendritic solidification and grain  
594 refiner potency characterised through in situ X-radiography, *Acta Mater.* 95 (2015) 83-89.

595 [30] A. Bogno, H. Nguyen-Thi, B. Billia, G. Reinhart, N. Mangelinck-Noel, N. Bergeon, T. Schenk, J. Baruchel, Iop,  
596 In situ and real-time analysis of the growth and interaction of equiaxed grains by synchrotron X- ray radiography,  
597 3rd International Conference on Advances in Solidification Processes, Iop Publishing Ltd, Bristol, 2012.

598 [31] M. Becker, S. Klein, F. Kargl, In-situ solute measurements with a laboratory polychromatic microfocus X-ray  
599 source during equiaxed solidification of an Al-Ge alloy, *Scr. Mater.* 124 (2016) 34-37.

600 [32] N. Shevchenko, O. Roshchupkina, O. Sokolova, S. Eckert, The effect of natural and forced melt convection on  
601 dendritic solidification in Ga-In alloys, *Journal of Crystal Growth* 417 (2015) 1-8.

602 [33] M. Becker, C. Dreissgacker, S. Klein, F. Kargl, Near-isothermal furnace for in situ and real time X-ray  
603 radiography solidification experiments, *Review of Scientific Instruments* 86(6) (2015).

604 [34] A.G. Murphy, D.J. Browne, W.U. Mirihanage, R.H. Mathiesen, Combined in situ X-ray radiographic  
605 observations and post-solidification metallographic characterisation of eutectic transformations in Al-Cu alloy  
606 systems, *Acta Mater.* 61(12) (2013) 4559-4571.

607 [35] C. Rakete, C. Baumbach, A. Goldschmidt, D. Samberg, C.G. Schroer, F. Breede, C. Stenzel, G. Zimmermann, C.  
608 Pickmann, Y. Houltz, C. Lockowandt, O. Svenonius, P. Wiklund, R.H. Mathiesen, Compact x-ray microradiograph  
609 for in situ imaging of solidification processes: Bringing in situ x-ray micro-imaging from the synchrotron to the  
610 laboratory, *Review of Scientific Instruments* 82(10) (2011).

611 [36] L. Abou-Khalil, G. Salloum-Abou-Jaoude, G. Reinhart, C. Pickmann, G. Zimmermann, H. Nguyen-Thi, Influence  
612 of gravity level on Columnar-to-Equiaxed Transition during directional solidification of Al – 20 wt.% Cu alloys, *Acta*  
613 *Mater.* 110 (2016) 44-52.

614 [37] D.J. Browne, F. Garcia-Moreno, H. Nguyen-Thi, G. Zimmermann, F. Kargl, R.H. Mathiesen, A. Griesche, O.  
615 Minster, Overview of In Situ X-Ray Studies of Light Alloy Solidification in Microgravity, in: K.N. Solanki, D. Orlov, A.  
616 Singh, N.R. Neelameggham (Eds.), *Magnesium Technology 2017*, Springer International Publishing Ag, Cham,  
617 2017, pp. 581-590.

618 [38] A. Buffet, H. Nguyen Thi, A. Bogno, T. Schenk, N. Mangelinck-Noël, G. Reinhart, N. Bergeon, B. Billia, J.  
619 Baruchel, Measurement of solute profiles by means of synchrotron X-ray radiography during directional  
620 solidification of Al - 4 wt% Cu alloys, *Materials Science Forum* 649 (2010) 331-336.

621 [39] H. Soltani, G. Reinhart, M.C. Benoudia, F. Ngomesse, M. Zahzouh, H. Nguyen-Thi, Impact of growth velocity  
622 on grain structure formation during directional solidification of a refined Al-20 wt.%Cu alloy, *Journal of Crystal  
623 Growth* 548 (2020) 125819.

624 [40] A.L. Greer, A.M. Bunn, A. Tronche, P.V. Evans, D.J. Bristow, Modelling of inoculation of metallic melts:  
625 application to grain refinement of aluminium by Al-Ti-B, *Acta Mater.* 48(11) (2000) 2823-2835.

626 [41] M. Abramoff, P. Magalhães, S.J. Ram, Image Processing with ImageJ, *Biophotonics International* 11 (2003)  
627 36-42.

628 [42] V.B. Biscuola, M.A. Martorano, Mechanical Blocking Mechanism for the Columnar to Equiaxed Transition,  
629 *Metallurgical and Materials Transactions a-Physical Metallurgy and Materials Science* 39A(12) (2008) 2885-2895.

630 [43] H. Nguyen-Thi, G. Reinhart, N. Mangelinck-Noël, H. Jung, B. Billia, T. Schenk, J. Gastaldi, J. Härtwig, J. Baruchel,  
631 In-Situ and Real-Time Investigation of Columnar-to-Equiaxed Transition in Metallic Alloy, *Metallurgical and  
632 Materials Transactions A* 38(7) (2007) 1458-1464.

633 [44] A. Prasad, S.D. McDonald, H. Yasuda, K. Nogita, D.H. StJohn, A real-time synchrotron X-ray study of primary  
634 phase nucleation and formation in hypoeutectic Al-Si alloys, *Journal of Crystal Growth* 430 (2015) 122-137.

635 [45] Y.J. Xu, D. Casari, R.H. Mathiesen, Y.J. Li, Revealing the heterogeneous nucleation behavior of equiaxed grains  
636 of inoculated Al alloys during directional solidification, *Acta Mater.* 149 (2018) 312-325.

637 [46] Y. Jia, D. Wang, Y. Fu, A. Dong, G. Zhu, D. Shu, B. Sun, In situ Investigation of the Heterogeneous Nucleation  
638 Sequence in Al-15 Weight Percent Cu Alloy Inoculated by Al-Ti-B, *Metallurgical and Materials Transactions A* 50(4)  
639 (2019) 1795-1804.

640 [47] H. Soltani, G. Reinhart, M.C. Benoudia, M. Zahzouh, H. Nguyen-Thi, Impact of gravity-related phenomena on  
641 the grain structure formation: comparative study between horizontal and vertical solidification of a refined Al-  
642 20wt.%Cu alloy, *IOP Conference Series: Materials Science and Engineering* 529 (2019) 012019.

643 [48] J.D. Hunt, Steady State Columnar and Equiaxed Growth of Dendrites and Eutectic, *Materials Science and  
644 Engineering* 65 (1984) 75-83.

645 [49] S. Ganesan, D.R. Poirier, Densities of Aluminum-Rich Aluminum-Copper Alloys during Solidification,  
646 *Metallurgical Transaction A* 18A (1987) 721-723.

647 [50] H. Nguyen-Thi, G. Reinhart, G. Salloum-Abou-Jaoude, D.J. Browne, A.G. Murphy, Y. Houltz, J. Li, D. Voss, A.  
648 Verga, R.H. Mathiesen, G. Zimmermann, XRMON-GF Experiments Devoted to the in Situ X-ray Radiographic  
649 Observation of Growth Process in Microgravity Conditions, *Microgravity Science and Technology* 26(1) (2014) 37-  
650 50.

651 [51] T. Nelson, B. Cai, N. Warnken, P.D. Lee, E. Boller, O.V. Magdysyuk, N.R. Green, Gravity effect on thermal-solutal  
652 convection during solidification revealed by four-dimensional synchrotron imaging with compositional mapping,  
653 *Scr. Mater.* 180 (2020) 29-33.

654 [52] M.D. Dupouy, D. Camel, J.J. Favier, Natural convective effects in directional dendritic solidification of binary  
655 metallic alloys: dendritic array morphology, *Journal of Crystal Growth* 126(2-3) (1993) 480-492.

656 [53] A. Olmedilla, M. Zaloznik, H. Combeau, Quantitative 3D mesoscopic modeling of grain interactions during  
657 equiaxed dendritic solidification in a thin sample, *Acta Mater.* 173 (2019) 249-261.

658 [54] G. Zimmermann, C. Pickmann, M. Hamacher, E. Schaberger-Zimmermann, H. Neumann-Heyme, K. Eckert, S.  
659 Eckert, Fragmentation-driven grain refinement in directional solidification of AlCu10wt-% alloy at low pulling  
660 speeds, *Acta Mater.* 126 (2017) 236-250.

661 [55] A. Saad, C.-A. Gandin, M. Bellet, N. Shevchenko, S. Eckert, Simulation of Channel Segregation During  
662 Directional Solidification of In—75 wt pct Ga. Qualitative Comparison with In Situ Observations, *Metallurgical and*  
663 *Materials Transactions A* 46(11) (2015) 4886-4897.

664 [56] S.M. Copley, A.F. Giamei, S.M. Johnson, M.F. Hornbecker, The origin of freckles in unidirectionally solidified  
665 castings, *Metallurgical Transactions* 1(8) (1970) 2193-2204.

666 [57] A. Hellawell, J.R. Sarazin, R.S. Steube, Channel Convection in Partly Solidified Systems, *Philosophical*  
667 *Transactions of the Royal Society of London Series a-Mathematical Physical and Engineering Sciences* 345(1677)  
668 (1993) 507-544.

669 [58] L. Hachani, B. Saadi, X.D. Wang, A. Nouri, K. Zaidat, A. Belgacem-Bouzida, L. Ayouni-Derouiche, G. Raimondi,  
670 Y. Fautrelle, Experimental analysis of the solidification of Sn–3 wt.%Pb alloy under natural convection,  
671 *International Journal of Heat and Mass Transfer* 55 (7) (2012) 1986-1996.

672 [59] S. Boden, S. Eckert, G. Gerbeth, Visualization of freckle formation induced by forced melt convection in  
673 solidifying GaIn alloys, *Materials Letters* 64(12) (2010) 1340-1343.

674 [60] G. Reinhart, D. Grange, L. Abou-Khalil, N. Mangelinck-Noël, N.T. Niane, V. Maguin, G. Guillemot, C.A. Gandin,  
675 H. Nguyen-Thi, Impact of solute flow during directional solidification of a Ni-based alloy: In-situ and real-time X-  
676 radiography, *Acta Mater.* 194 (2020) 68-79.

677 [61] L. Yuan, P.D. Lee, A new mechanism for freckle initiation based on microstructural level simulation, *Acta*  
678 *Mater.* 60(12) (2012) 4917-4926.

679 [62] A. Bogno, H. Nguyen-Thi, G. Reinhart, B. Billia, J. Baruchel, Growth and interaction of dendritic equiaxed  
680 grains: In situ characterization by synchrotron X-ray radiography, *Acta Mater.* 61(4) (2013) 1303-1315.

681 [63] Y. Fautrelle, J. Wang, G. Salloum-Abou-Jaoude, L. Abou-Khalil, G. Reinhart, X. Li, Z. Ren, H. Nguyen-Thi,  
682 Thermo-Electric-Magnetic Hydrodynamics in Solidification: In Situ Observations and Theory, *JOM Journal of the*  
683 *Minerals, Metals and Materials Society* 70(5) (2018) 764 - 771.

684

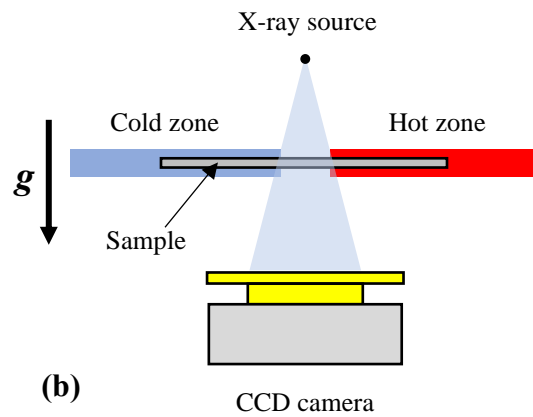
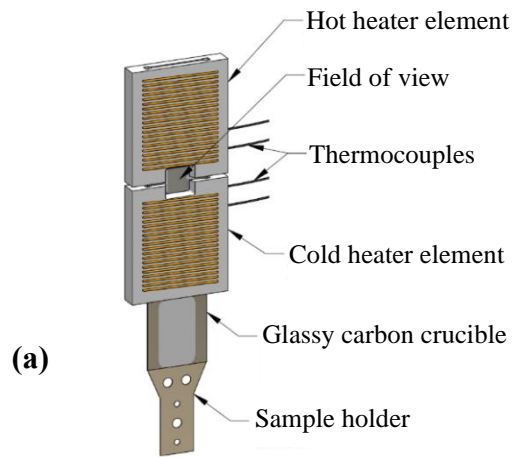


Fig. 1: Schematic layout of (a) the SFINX furnace (courtesy of A. G. Murphy, UCD), and (b) the SFINX experimental arrangement (furnace and X-radiography system) for horizontal solidification experiment.



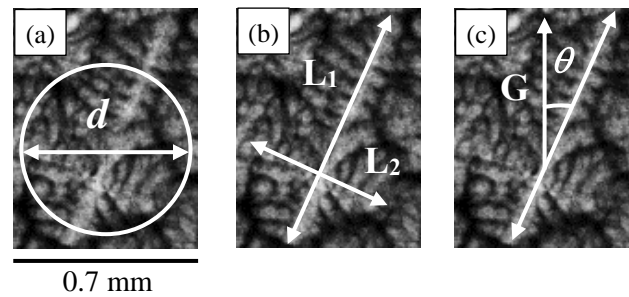


Fig. 2: Dendritic grain characteristics measured in the present paper: (a) Diameter  $d$  of the equivalent disk, (b)  $L_1$  length of the longest straight segment in the grain and  $L_2$  length of the longest straight segment in the grain and orthogonal to the segment  $L_1$ , (c) tilt angle  $\theta$  between the temperature gradient direction and the main dendrite axis.

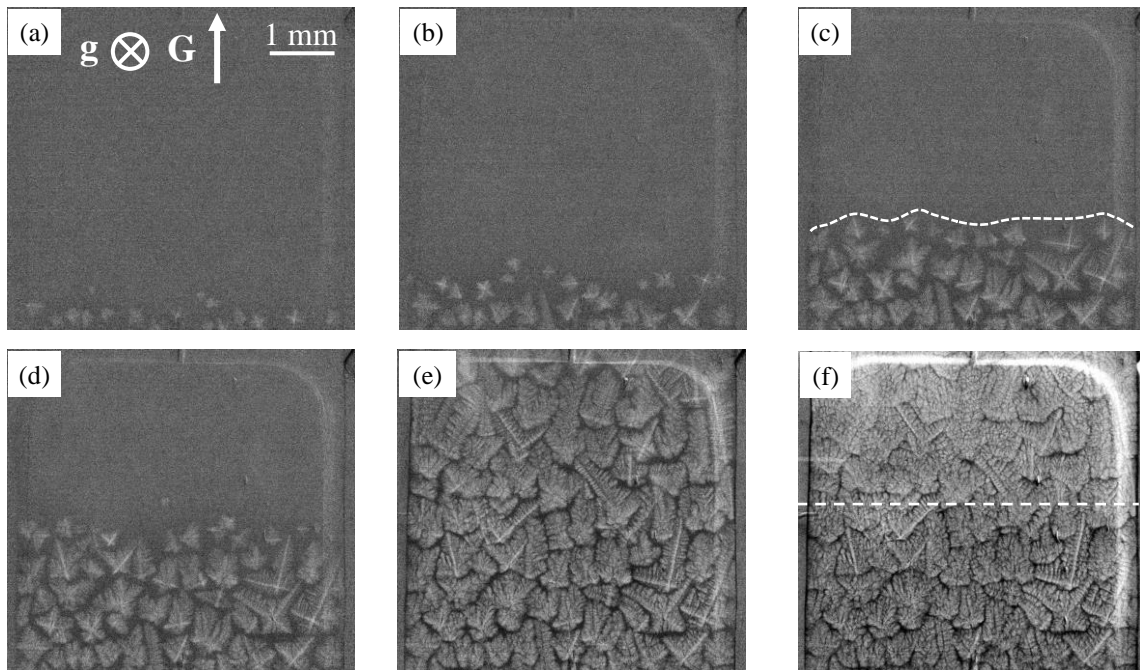


Fig. 3: Sequence of radiographs recorded during the solidification experiment A1 (refined Al-20wt.%Cu in horizontal configuration,  $\langle V_N \rangle = 25.4 \mu\text{m/s}$  and  $\langle G_N \rangle = 5.9 \text{ K/mm}$ ), showing the propagation of the solidification microstructure. (The reference time  $t = 0 \text{ s}$  is chosen at the beginning of the temperature decrease: a)  $t = 135 \text{ s}$ , b)  $t = 151 \text{ s}$ , c)  $t = 179 \text{ s}$  (the dashed line points out the effective solidification front), d)  $t = 202 \text{ s}$ , e)  $t = 337 \text{ s}$ , f)  $t = 562 \text{ s}$  (the dashed line shows the eutectic front crossing the Field-of-View).

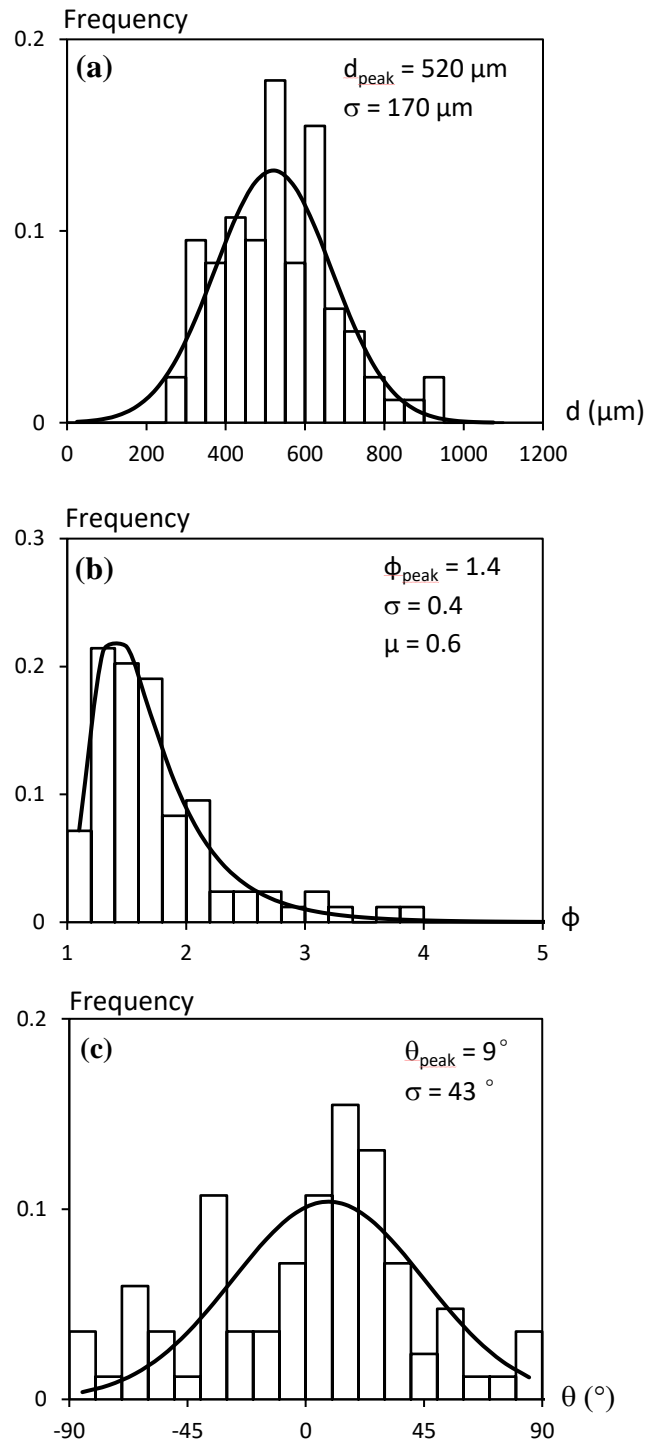


Fig. 4: Distributions of (a) grain size, (b) grain elongation and (c) growth orientation for the experiment A1 (horizontal solidification of a refined Al-20wt.%Cu,  $\langle V_N \rangle = 25.4 \mu\text{m/s}$  and  $\langle G_N \rangle = 5.9 \text{ K/mm}$ ).

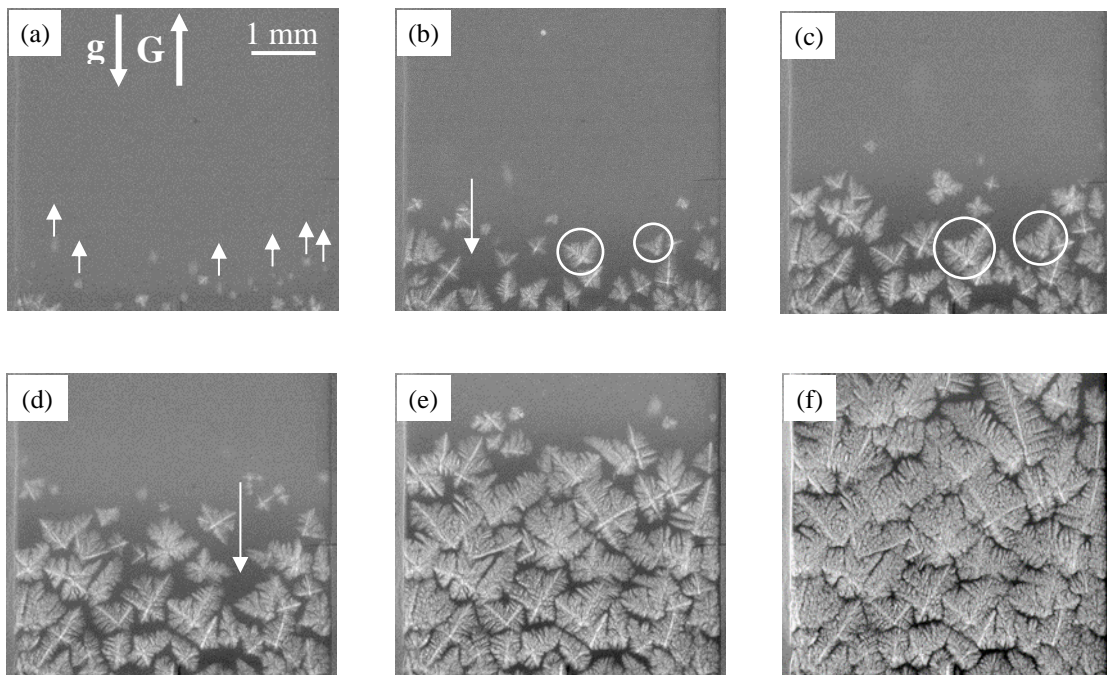


Fig. 5: Sequence of radiographs recorded during the upward solidification B2 (refined Al-20 wt.%Cu,  $\langle V_N \rangle = 23.4 \mu\text{m/s}$  and  $\langle G_N \rangle = 6.4 \text{ K/mm}$ ). The reference time  $t = 0 \text{ s}$  is chosen at the beginning of the temperature decrease: a)  $t = 13 \text{ s}$  (upward white arrows indicate the motion of the grains) , b)  $t = 30 \text{ s}$  (the downward white arrow indicates a residual liquid area formed between grains and white circles show two stuck grains), c)  $t = 47 \text{ s}$  (white circles show two stuck grains), d)  $t = 58 \text{ s}$  (the downward white arrow indicates a residual liquid area formed between grains), e)  $t = 92 \text{ s}$ , f)  $t = 153 \text{ s}$ .

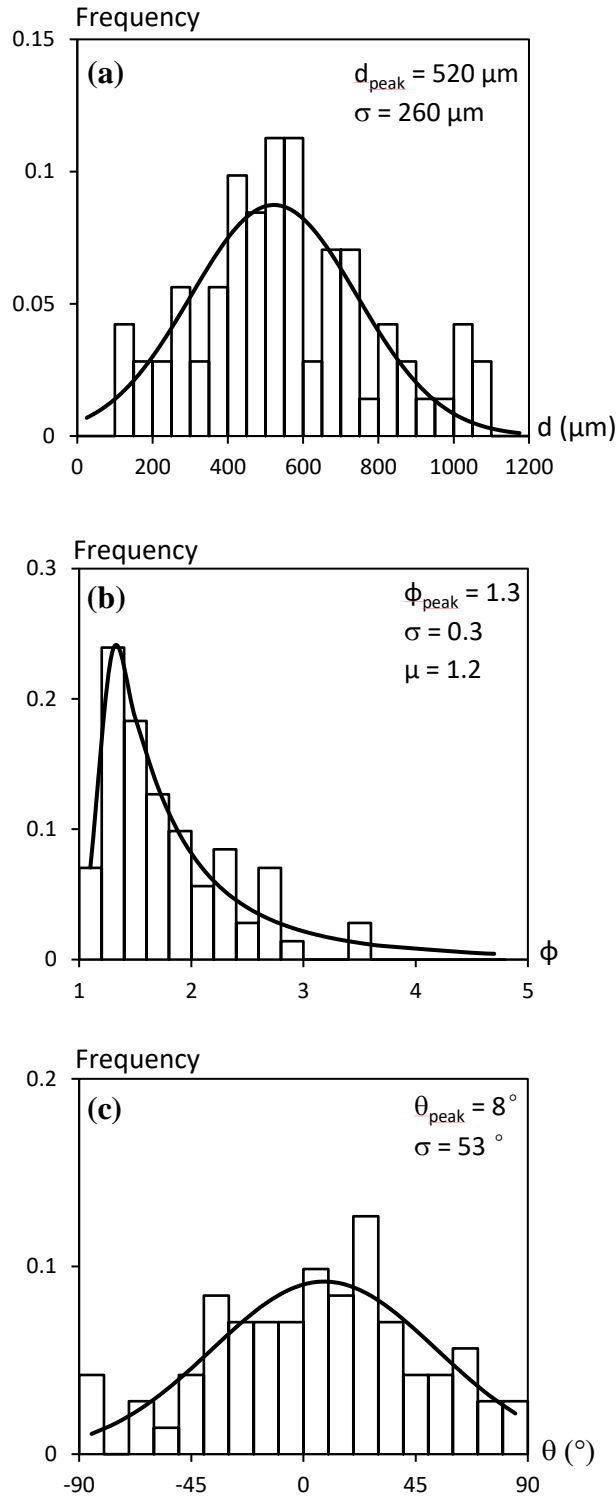


Fig. 6: Distributions of (a) grain size, (b) grain elongation and (c) growth orientation for the vertical upward configuration in the B2 case (refined Al-20wt.%Cu,  $\langle V_N \rangle = 23.4 \mu\text{m/s}$  and  $\langle G_N \rangle = 6.4 \text{ K/mm}$ ).



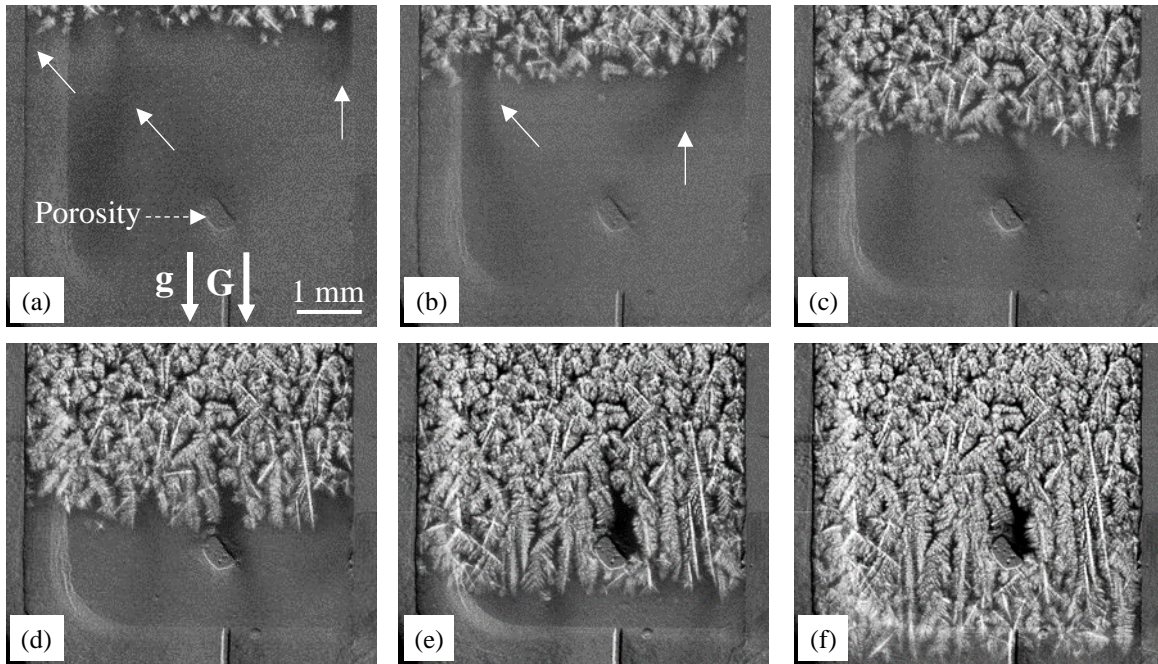


Fig. 7: Sequence of radiographs recorded during the experiment C1 (downward solidification of a refined Al-20wt.%Cu,  $\langle V_N \rangle = 22.2 \mu\text{m/s}$  and  $\langle G_N \rangle = 6.8 \text{ K/mm}$ ), showing the propagation of the solidification microstructure from the top-cold zone toward the bottom-hot zone of the sample. The plain white arrows show solute plume locations. The reference time  $t = 0 \text{ s}$  is chosen at the beginning of the temperature decrease: a)  $t = 175 \text{ s}$ , b)  $t = 218 \text{ s}$ , c)  $t = 280 \text{ s}$ , d)  $t = 333 \text{ s}$ , e)  $t = 420 \text{ s}$ , f)  $t = 491 \text{ s}$ .

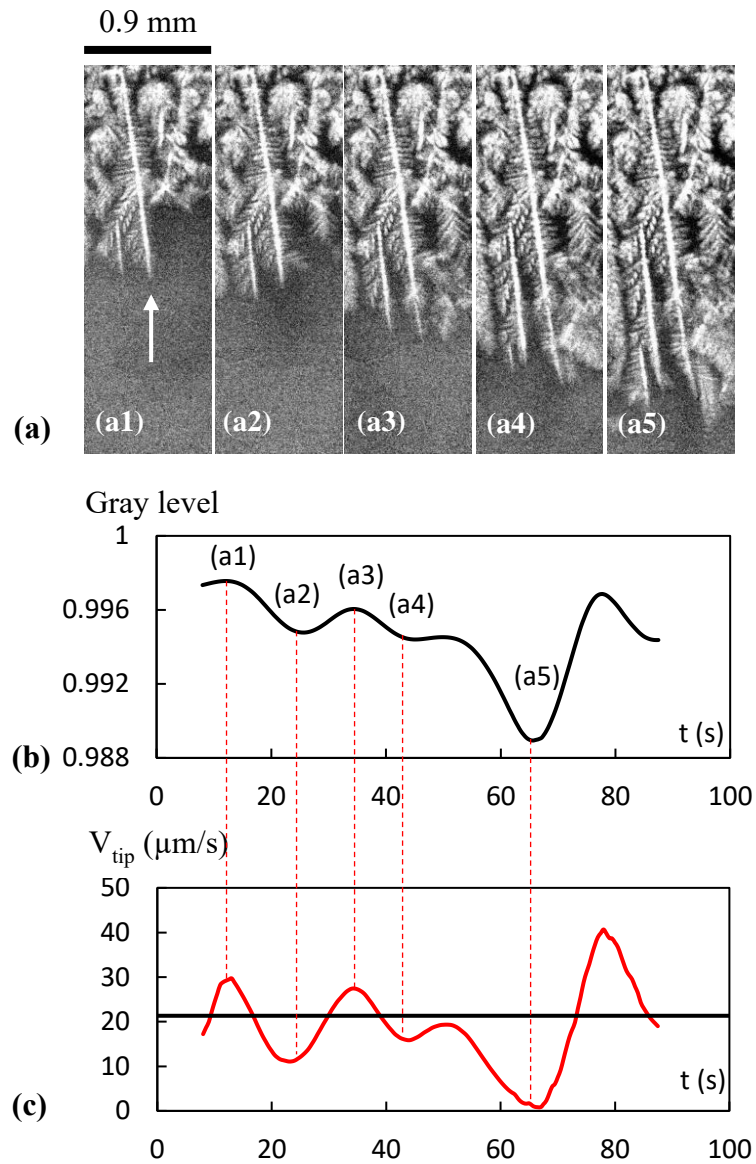


Fig. 8: (a) Sequence of radiographs of a dendrite development during the experiment C1 (downward solidification of a refined Al-20wt.%Cu,  $\langle V_N \rangle = 22.2 \mu\text{m/s}$  and  $\langle G_N \rangle = 6.8 \text{ K/mm}$ ) at (a1)  $t = 288 \text{ s}$ , (a2)  $t = 298 \text{ s}$ , (a3)  $t = 311 \text{ s}$ , (a4)  $t = 334 \text{ s}$  and (a5)  $t = 352 \text{ s}$  (the reference time  $t = 0 \text{ s}$  is chosen at the beginning of the cooling). (b) Gray level variation in front of the dendrite tip and (c) variation of the tip velocity for the dendrite indicated by a white arrow in the first radiograph.



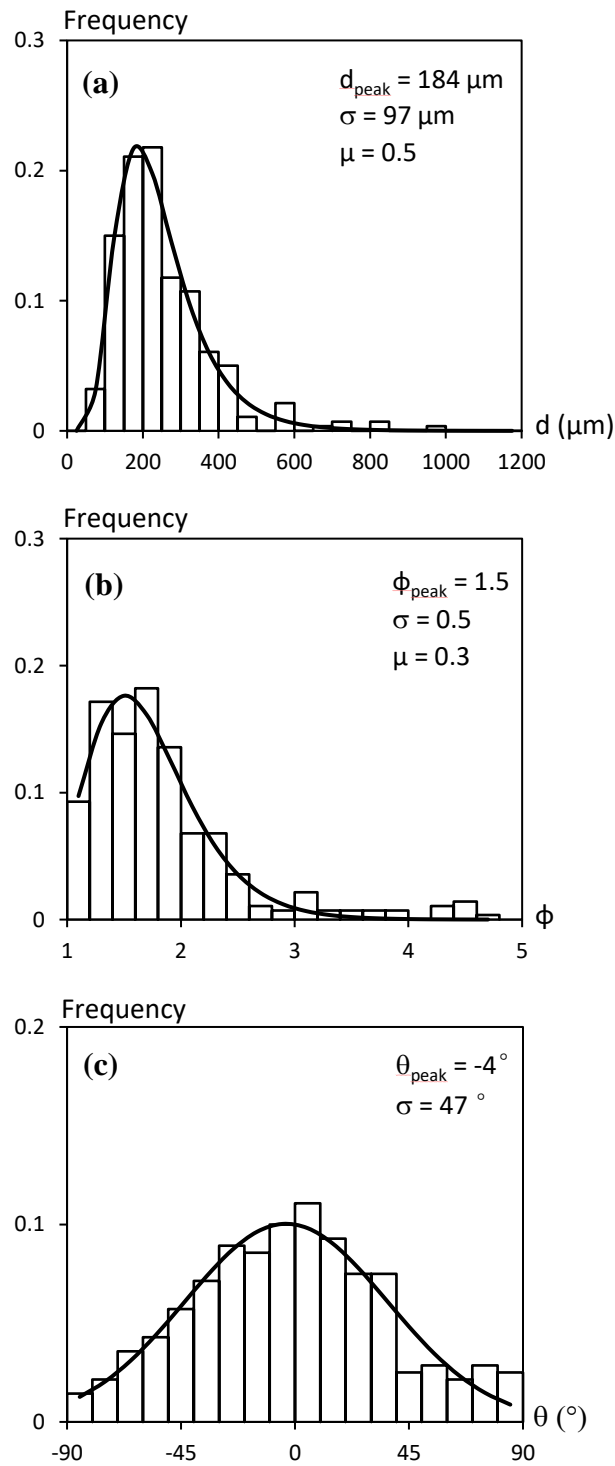


Fig. 9: Distributions of (a) grain size, (b) grain elongation and (c) growth orientation for the C1 experiment (downward solidification of a refined Al-20wt.%Cu,  $\langle V_N \rangle = 22.2 \mu\text{m/s}$  and  $\langle G_N \rangle = 6.8 \text{ K/mm}$ ).

	Experiment	$\langle V_N \rangle$ ( $\mu\text{m/s}$ )	$\langle V_E \rangle$ ( $\mu\text{m/s}$ )	$\langle G_N \rangle$ (K/mm)	$\langle G_E \rangle$ (K/mm)
<b>Case A</b> Horizontal solidification	A1	25.4	27.8	5.9	5.4
	A2	24.5	27.2	6.1	5.5
<b>Case B</b> Upward solidification	B1	24.5	-	6.1	-
	B2	23.4	-	6.4	-
	B3	23.9	-	6.3	-
	B4	22.9	26.5	6.6	5.7
	B5	23.3	27.6	6.4	5.4
	B6	25.7	29.1	5.8	5.2
<b>Case C</b> Downward solidification	C1	22.2	24.7	6.8	6.1
	C2	22.3	24.5	6.7	6.1
	C3	20.2	24.4	7.4	6.1

Table 1 Measured average values of the nucleation front velocity  $\langle V_N \rangle$ , eutectic front velocity  $\langle V_E \rangle$ , nucleation temperature gradient  $\langle G_N \rangle$  and eutectic temperature gradient  $\langle G_E \rangle$  for the three series of solidification experiment on refined Al-20wt.%Cu alloys.